Journal of The Electrochemical Society, **165** (10) A1-A10 (2018)
0013-4651/2018/165(10)/A1/10/$37.00 © The Electrochemical Society

Efficient Capacitive Deionization Using Thin Film Sodium Manganese Oxide

Jasmine M. Wallas,[1] Matthias J. Young,[2,3,z] Huaxing Sun,[1] and Steven M. George[1,4,z]

[1]*Department of Chemistry and Biochemistry, University of Colorado, Boulder, Colorado 80309,USA*
[2]*Applied Chemicals and Materials Division, National Institute of Standards and Technology, Boulder, Colorado 80305,USA*
[3]*Energy Systems, Argonne National Laboratory, Argonne, Illinois 60439, USA*
[4]*Department of Mechanical Engineering, University of Colorado, Boulder, Colorado 80309, USA*

More energy efficient desalination methods are needed to address global water scarcity. Capacitive deionization (CDI) is an emerging electrochemical desalination technology that could outperform other desalination technologies if new electrode materials were developed with high salt sorption capacity and efficiency. In this paper, we report on the desalination performance of thin-film sodium manganese oxide (NMO). We deposit thin-film MnO via atomic layer deposition (ALD), and electrochemically convert the MnO to NMO in $NaCl_{(aq)}$. Charge storage capacity is tuned with NMO thickness, and the relationship between charge storage capacity and reversible salt sorption is probed. NMO coated electrodes exhibit increases in charge storage capacity up to 170 times higher than uncoated electrodes. Electrochemical quartz crystal microbalance (EQCM) measurements reveal that thin-film NMO leads to the efficient electrochemical removal of Na^+ ions. A hybrid CDI (HCDI) cell comprised of NMO-coated carbon nanotube (CNT) cathode and Ag nanoparticle-decorated CNT anode yields a ~20-fold improvement in charge storage over bare CNT electrodes. The HCDI cell has an anomalously high reversible charging efficiency, which we study using ab initio modeling and EQCM. This is the first CDI report using thin film NMO, and the high desalination efficiency we identify promises to facilitate the development of HCDI devices with enhanced performance.
 [DOI: 10.1149/2.0751810jes]

Manuscript submitted April 13, 2018; revised manuscript received July 2, 2018. Published 00 0, 2018.

Fresh drinking water is becoming increasingly scarce around the globe, intensifying the need for energy efficient desalination methods that could be powered with renewable energy sources.[1] The need for fresh drinking water tops the list of *50 Breakthroughs: Critical scientific and technological advances needed for sustainable global development* compiled by the Institute of Globally Transformative Technologies at Lawrence Berkeley National Lab.[2] Capacitive deionization (CDI) is a promising water desalination technique based on the reversible electrosorption of ions. Unlike other desalination techniques, CDI requires only a nominal voltage, and therefore could easily be coupled with solar power or other renewable energy sources.

During CDI operation, the electrical potential across two electrodes is cycled between two modes, a 'desalination' half cycle and a 'regeneration' half cycle. During the desalination half cycle of a traditional CDI cell an electrical potential is applied to the CDI cell, causing ion sorption to the electrodes and producing fresh water. During the regeneration half cycle of a traditional CDI cell the polarization is reduced or reversed and ions desorb from the electrodes, thereby regenerating the electrodes and producing brine. Conventionally, CDI electrodes are composed of inert carbon. In these carbon electrodes, energy is stored during the desalination step by ion sorption in the electric double layer (EDL), and some of this energy can be recovered during regeneration. This unique behavior lowers the overall net energy consumption of CDI, particularly for desalination of low salinity feed waters.[3]

To compete with commercial desalination technologies used for higher salinities (e.g. reverse osmosis), CDI costs must be reduced. At present CDI is viable at saltwater concentrations below ~ 0.05 M, well below the salinity levels of seawater.[3,4] Carbon electrodes currently used in CDI have low salt sorption capacity (SSC) (units in mg NaCl (g electrode)$^{-1}$), limited to the available surface area for EDL ion sorption. Low salt sorption capacity leads to larger devices with higher capital costs. Additionally, low salt sorption capacity materials require larger composite electrode thicknesses, which introduce ohmic and diffusion losses and limit the efficiency of conventional CDI.

By increasing the capacity of CDI electrode materials, smaller devices can be constructed using thinner electrodes, which will reduce capital costs and provide lower operating costs through greater energy efficiency. Consequently, hybrid CDI (HCDI) electrodes that incorporate ion intercalation materials commonly used in batteries and supercapacitors have been explored and have shown to improve performance.[5–7] These materials often have higher charge storage capacities (CSC) (with units of F g^{-1} or F cm^{-2}) than carbon electrodes, and exhibit low self-discharge rates.[8] The use of ion-selective intercalation materials is expected to increase charge efficiency ($\wedge$ = mol NaCl (mol e-)$^{-1}$) by reducing the energetic contribution of co-ion desorption during the charging half-cycle, and to increase the coulombic efficiency (η = mol $e_{regeneration}$/mol $e_{desalination}$) due to the low self-discharging properties of these materials.

Manganese oxide, used as a reversible Na^+ intercalation material in Na-ion batteries,[9–11] is a promising candidate for increasing the SSC of HCDI electrodes. Recent studies have confirmed that the CSC of MnO_2 in aqueous Na^+ solutions is largely due to cation (i.e. Na^+) sorption and intercalation.[12–17] Several reports have investigated the incorporation of sodium manganese oxide (NMO) particles into HCDI electrodes, demonstrating modest improvements in SSC.[6,7,18–20] Using an NMO electrode, Lee et al. achieved the highest HCDI SSC at 31.2 $mg_{(salt)}/g_{(electrode)}$, more than twice that of the highest SSC reported for a conventional CDI system.[4,7] This increase in SSC was achieved by adding $Na_{0.44}MnO_2$ particles into the cell's carbon cathode. However, this factor of two increase falls well short of the factor of ten improvement expected when comparing NMO CSC versus carbon CSC, suggesting that the advantages of NMO may not have been fully realized in these studies.[21,22]

Here we describe the study of Na^+ intercalation and charge storage in nanoscale thin films of NMO formed with a controlled two-step process – atomic layer deposition (ALD) of MnO, followed by electrochemical oxidation to form NMO – and provide an initial study of its potential application to enhance HCDI. This work expands on previous work from our group, where NMO was formed from MnO in $Na_2SO_{4(aq)}$.[13] Here, we electrochemically convert MnO to NMO in $NaCl_{(aq)}$ to mimic industrially relevant feed water for eventual simplified deployment in HCDI devices. By measuring the CSC versus thickness after conversion to NMO, we probe the depth to which MnO is oxidized to NMO in $NaCl_{(aq)}$. We use these results to produce HCDI cathodes with a starting MnO thickness tuned to produce the highest possible capacity.

We compare cycling performance of a conventional CDI configuration consisting of two carbon nanotube (CNT) electrodes and an HCDI configuration where the CNT cathode is coated with NMO, as described above, and the CNT anode is decorated with Ag

[z]E-mail: Matthias.Young@anl.gov; Steven.George@colorado.edu

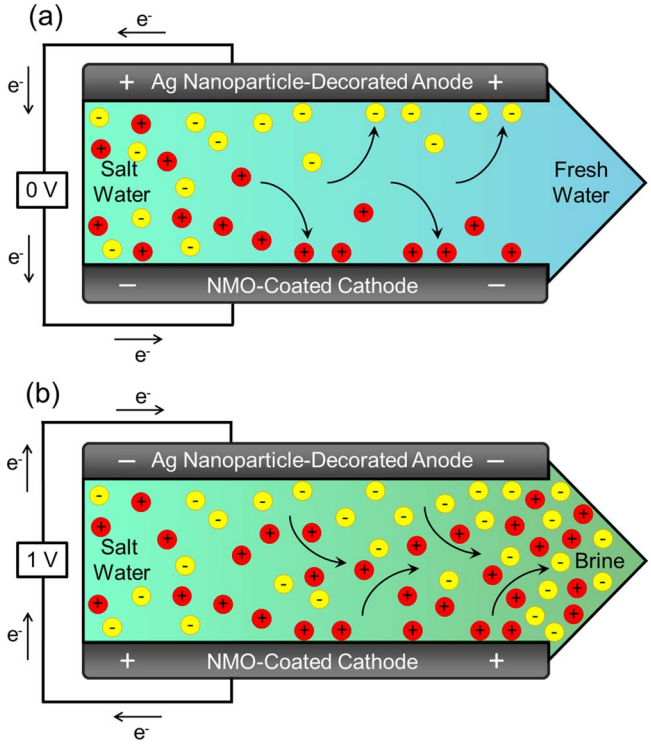

Figure 1. Schematic diagram of hybrid capacitive deionization (HCDI) with an NMO coated cathode and Ag nanoparticle decorated anode. (a) In our HCDI cell desalination occurs with an applied potential of 0 V, where solvated Na^+ ions intercalate into the NMO cathode and solvated Cl^- ions react with Ag to form AgCl, yielding fresh water. (b) Regeneration in our HCDI cell occurs with an applied positive potential, where Na^+ is released from the NMO cathode and Cl^- is released from the AgCl anode, producing a brine solution and restoring the electrodes to their initial state.

nanoparticles. The desalination mechanism of this HCDI cell differs from traditional CDI and is shown in Figure 1. This work contrasts prior studies on HCDI electrodes that exclusively used particulate active material. The use of a conformal NMO thin-film coating is expected to enhance performance by increasing electrical connectivity[23] and decreasing the diffusion lengths required for Na^+ to access the NMO. This HCDI cell exhibits low net energy consumption and high charging efficiency (mol NaCl (mol e-)$^{-1}$). We explore the relationship between charge storage and salt sorption in NMO using EQCM and ab initio modeling to understand the high efficiency we observe.

Experimental

Electrode fabrication.—Electrodes for the conventional CDI test cell were composed of multi-walled hydroxylated carbon nanotubes (CNT-OH) (> 95%, 10–20 nm OD, > 200 m^2/g, Nanostructured and Amorphous Materials, Inc.) with a 20% by weight poly(vinyldene fluoride) (PVDF) (M_w ~ 530,000, Aldrich) binder on titanium (Ti) discs (99.6%, annealed, 0.5 mm, Goodfellow) cut to a 4 cm diameter with electron discharge machining before coating. Hydroxyl-functionalized CNTs were used to promote ALD nucleation, while binder mass loadings of 20% were used in the electrodes to support mechanical stability during volume expansion in NMO conversion[13] and Ag/AgCl reaction. Ti substrate was used for electrochemical testing due to its conductivity and corrosion resistance in $NaCl_{(aq)}$.[24]

A slurry composed of 8 mg/mL CNT-OH and 2 mg/mL PVDF in 1-methyl-2-pyrrolidinone (ACS reagent, ≥ 99.0%, Sigma-Aldrich) was coated onto a Ti disc at 25 μL/cm^2, corresponding to 0.2 mg/cm^2 CNT-OH. Films were heated to ~ 80°C overnight to dry. The cathode in the HCDI cell was assembled in the same fashion as described above, and then coated using ALD as described in the Supplementary Information (SI) Section A. The anode in the HCDI cell was supplemented with silver nanopowder (Ag NP) (< 100 nm particle size, PVP dispersant, 99.5% trace metals basis, Aldrich) to avoid capacity limitations while studying the NMO electrodes. A slurry of 78 mg/mL Ag NP, 20 mg/mL PVDF, and 2 mg/mL CNTs (7000 series, Nanocyl) was coated onto a Ti disc at 80 μL/cm^2. Assembled composite electrodes were allowed to wet in the electrolyte solution for ~ 8 hours before electrochemical testing in order to avoid progressive wetting effects.

NMO formation by ALD and electrochemical conversion.—We followed procedures analogous to those described previously for ALD of MnO;[13,25] and electrochemical conversion of MnO to NMO.[13] See SI for details of electrochemical three-electrode setup and MnO conversion.

X-Ray photoelectron spectroscopy.—Film composition was characterized with X-ray photoelectron spectroscopy (XPS). XPS was conducted using a PHI 5600 X-ray photoelectron spectrometer (RBD Instruments) with a monochromatic Al-Kα X-ray source at 1486.6 eV. Depth profiling was accomplished with 90s argon ion sputtering intervals between spectra acquisitions. Spectra were obtained using a pass energy of 29.35 eV, a step size of 0.25 eV, and Auto-Neutralization mode. AugerScan control program (RBD Instruments) was used to collect data, and CasaXPS software (Casa Software) was used to analyze XPS data.

Electrochemical quartz crystal microbalance.—Electrochemical quartz crystal microbalance (EQCM) was employed to evaluate mass changes due to ion sorption and intercalation during potential scans. MnO ALD films were deposited as described in the SI onto Pt-plated EQCM crystals (1" diameter, AT-cut quartz crystal wafer, Stanford Research Systems). Electrochemistry was conducted in a custom glass electrochemical cell attached to an EQCM crystal holder (Stanford Research Systems) with a Pt counter and saturated Ag/AgCl reference electrode in 0.10 M $NaCl_{(aq)}$ electrolyte. Film oxidation and capacity measurements were performed as described in the SI.

EQCM resonator frequency was recorded with a QCM200 (Stanford Research Systems) using a BioLogic potentiostat and control software. Mass changes (Δm) were calculated from frequency changes (Δf) using the simplified Sauerbrey equation, $\Delta m = 56.6\ \mu g\ (cm^2\ Hz)^{-1} \times \Delta f \times A$, where A is the surface area of the QCM crystal exposed to the electrolyte (1.37 cm^2). EQCM measurements were performed with capacitance compensation. The series resonant resistance was measured to be < 2 Ω in the NMO-coated EQCM experiments, indicating that dissipation effects are negligible for these films.[26,27]

Ab initio Modeling.—Electrochemistry of Na insertion in MnO_2 was modeled using the unified electrochemical band-diagram (UEB) framework, as described in prior work.[12,28] Here, we extend previous work[12] to model surface and bulk descriptions of insertion of Na into pristine α-MnO_2, as well as removal of Na from sodium-rich $NaMn_4O_8$, also in the α phase. Visualizations of these crystal structures are shown in Figure 2. We employ density functional theory (DFT) and the projector augmented-wave (PAW)[29] method as implemented in the Vienna Ab initio Simulation Package (VASP)[30–32] for electronic structure calculations. Pseudopotentials are used to describe core electrons, while chemically active sodium 2p and 3s, oxygen 2s and 2p, and manganese 3p, 3d, and 4s electrons are calculated explicitly using PAWs. A Γ-centered Monkhorst-Pack K-point mesh was generated for all structures using the fully automatic scheme in VASP with l = 14.

We correct for self-interaction error in defect calculations,[33,34] by employing the modified Heyd-Scuseria-Ernzerhof (HSEsol)[35] range-separated functional for charged defect calculations. We perform complete structural relaxations using multi-step cell-shape and ionic relaxations as implemented in *pylada*. Formation energies are calculated using the hydroxide-forming limit while accounting for pH and applied bias as described previously.[12] We note the

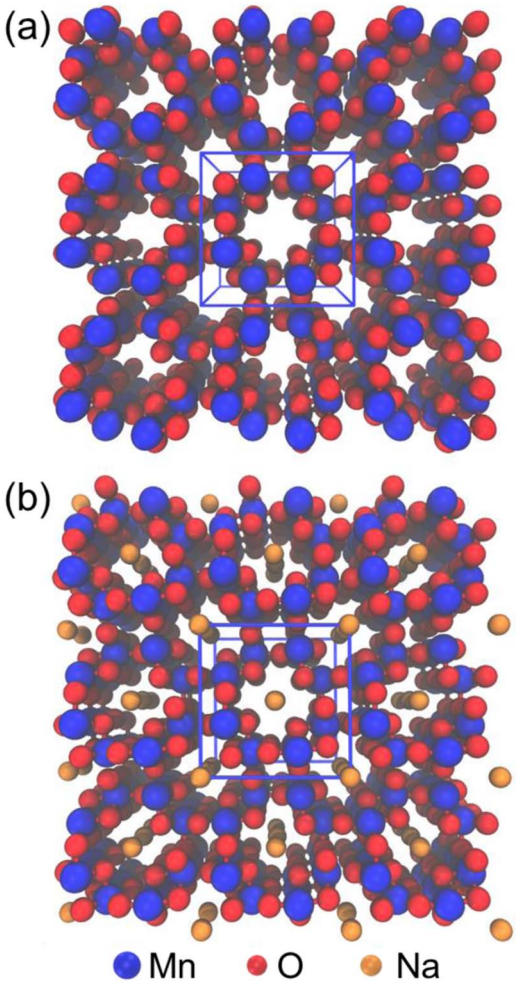

Figure 2. Visualization of crystal structures for ab initio modeling. (a) Structure of α-MnO_2. (b) Structure of $NaMn_4O_8$. These crystal structures were relaxed at an HSEsol level and used to model Na insertion into pristine MnO_2, and Na removal from sodium-rich $NaMn_4O_8$, respectively.

use of bulk crystal hydroxides rather than individual molecules for hydroxide reference calculations, as well as a sign correction in the applied bias as compared with this prior work. For surface descriptions, we account for band bending at the electrode surface using the point of zero charge according to $V = V_{PZC} + 0.059(pH_{PZC} - pH)$, as described previously,[12,36] using a pH_{PZC} value of 1.7 for cryptomelane.[37] Bulk descriptions in this work neglect this surface band bending and are expected to hold for depths into the active material larger than its characteristic Debye length.

Work function calculations were performed using the method of Fall et al.[38] with ≥ 17 Å thick slabs and ionic relaxation on all atoms > 5Å from the center plane of the slabs. Work functions were calculated at the revised Purdew-Burke-Ernzerhof (PBEsol)[39] level with band edge energies corrected at the HSEsol level, similar to work correcting band edge energies using quasiparticle calculations.[40] The work functions for [100], [001], and [110] surface terminations were averaged using a surface-energy weighted Boltzmann function to produce a single value of work function in line with a Wulff construction particle.

Desalination performance tests.—Desalination performance was evaluated with a custom HCDI cell, as shown in Figure 3. The HCDI cell is composed of two Ti discs (0.5 mm, 99.7%, annealed, Goodfellow) current collectors that were electron discharge machined to 4.0 cm diameter, thin CNT electrodes decorated with nanoscale materials, and a glass fiber separator (380 μm, EMD Millipore Glass Fiber Filter Grade AP20, Fisher Scientific). Tubing in and out of the cell was 1/16" ID PTFE. The HCDI cell was operated at a constant voltage, cycling between 0.0 and 1.0 V, with a cycle time of 30 minutes to allow sufficient time for salt sorption. The cell was operated in single-pass mode, with solution constantly flowing through the cell at a fixed rate. A long cycle time was used to ensure maximum desalination and regeneration values.

The cell was designed to detect the removal of small amounts of salt that arise from the sorption of ions into relatively small quantities of nanoscale material electrodes. Measurement of discrete changes in salt concentration was achieved by limiting the electrolyte volume of the cell and tubing, as depicted in Figure 3a, which prevents appreciable mixing between salt-depleted and salty electrolyte. We constrained the cell volume to 0.48 cm^3 to allow for desalination of multiple reservoir volumes based on estimates of SSC using NMO CSC data. The small electrolyte volume in the cell and tubing allowed us to measure desalination performance with smaller mass loadings of active material. Smaller mass loadings reduce the electrode thickness and minimize charge transfer resistance and diffusion effects, while maximizing electrode wetting. While most CDI test cells described in the literature use tens of mg/cm^2 of carbon material per electrode,[7,41,42] our cell is designed to require < 1 mg/cm^2 of carbon in each electrode. While this cell design is helpful for materials characterization and understanding, other cell designs are perhaps more practical for scale-up.[4,41,43]

In order to improve electrode/electrolyte contact, the HCDI cell was designed with a torturous electrolyte flow path. Each Ti disc was bored with a 1/16" diameter hole at 1 cm or 3 cm along the diameter for water feed through. These holes were placed opposite one another as depicted in Figure 3b, and electrolyte flow was directed through the opening in one Ti disc, across the separator, and out through the small opening on the opposite side of the cell in the second Ti disc. Flow was controlled with a Kent Scientific Genie Plus syringe pump with a 60 mL BD Luer-Lok syringe at a continuous flow rate of 0.200 mL/min. Both the pump and syringe flow rates are accurate to ± 1%, and the flow rate through the cell was manually verified by collecting the effluent in a graduated cylinder. Electrolyte concentration was 0.10 M $NaCl_{(aq)}$ and was drawn from a larger electrolyte volume of 1 L to ensure isothermal operation.

A 1/16" diameter flow-through conductivity meter (Microelectrodes, Inc.), positioned downstream of the cell, was used to monitor the salinity of the effluent solution and evaluate desalination performance. This low-volume conductivity probe, housed inside of a rigid low-volume case, allowed for continuous monitoring of the effluent salt concentration. Potential-controlled electrochemical impedance spectroscopy (PEIS) was used to monitor the impedance across the conductivity meter on the BioLogic potentiostat. A sine amplitude of 10.0 mV at a fixed potential of 200 mV was used for PEIS measurements, and the conductivity was evaluated at a frequency of 50 kHz to determine salt concentration. PEIS measurement values were subsequently converted to NaCl concentrations using calibration data. PEIS measurements were calibrated before and after each run using NaCl concentrations of 0.01, 0.10, and 1.00 M.

Results and Discussion

The first part of this work aimed to characterize the formation of NMO when oxidizing MnO thin films in aqueous NaCl electrolyte. Flat substrates and a three-electrode setup were used to study NMO formation to reduce the contribution of EDL charge storage and better understand Na^+ sorption processes in NMO. In the second part of this work, desalination capacity and efficiency of an HCDI cell containing an NMO-coated electrode were studied using the custom test cell (Figure 3). A high surface area NMO-coated CNT cathode was used in CDI tests to enhance the overall capacity. High surface area CNTs were chosen to enable reasonable desalination performance in the CDI cell and to provide sufficient surface area for MnO deposition. In the third part of this work, the relationship between charge storage and ion

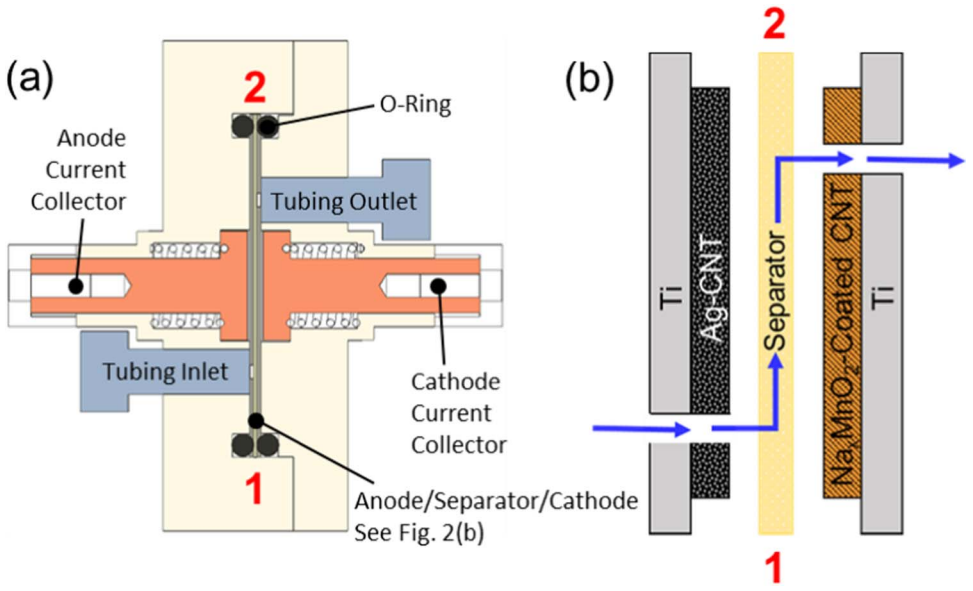

Figure 3. Depictions of hybrid capacitive deionization (HCDI) test cell. (a) Schematic of cut-away of test cell showing internal components, including the electrode assembly between labels 1 and 2. (b) Magnified schematic of electrode assembly, depicting the direction of water flow across the separator.

removal in NMO was further probed with EQCM and computational modeling.

NMO formation.—NMO film formation involved a two-step process of deposition and post-treatment, inspired by our previous work.[13] The growth rate of MnO ALD is 1.0 Å per deposition cycle on Ti in a viscous-flow configuration as measured by spectroscopic ellipsometry, and 2.1 Å per deposition cycle on silicon in a static configuration as measured by X-ray reflectivity (XRR). See SI section B for additional details. A higher growth rate in the static configuration as compared to the viscous configuration has been reported for other ALD chemistries, and may be explained by sub-saturation of the surface reactions during viscous growth.[44–46] The higher growth rate may also be explained by a CVD component to the growth, given the extended exposure times as compared with prior work[25] and low activation energies for decomposition of metal-cyclopentadienyl precursors on the order of ~25–35 kcal/mol.[47] Despite this possible CVD component, Field Emission Scanning Electron Microscopy (FESEM) of a composite CNT electrode coated with MnO suggests a uniform surface coating through the depth of the composite film (See SI Section D).

MnO films were post-processed with electrochemical oxidation in $NaCl_{(aq)}$. $NaCl_{(aq)}$ is used here in anticipation of the eventual development of MnO films in HCDI devices with in operando conversion to NMO during desalination of seawater or inland watershed. Conversion to NMO results in a large increase in CSC and a change in the visual appearance of the sample from a reflective green color (due to thin film interference) to a matte orange-brown, as shown in the photographs of the sample in Figure 4. The conversion of MnO to NMO in $NaCl_{(aq)}$ is qualitatively consistent with conversion seen previously in $Na_2SO_{4(aq)}$.[13]

We observe significant increases in CSC of NMO over bare Ti and MnO. These increases are consistent with conversion in $Na_2SO_{4(aq)}$.[13] CSC values are derived from cyclic voltammetry (CV) sweeps at 20 mV/s, as shown in Figure 4. See SI Section G for cycling stability over 300 CV sweeps. CSC values reported below are average values calculated for the full potential range during oxidizing sweeps. CSC values are normalized to either top-down surface area of the electrode exposed to the electrolyte (1.21 cm^2) for areal capacitance, or mass of NMO calculated from MnO thickness and density from XRR and assuming complete conversion to NMO for specific mass capacitance.

Bare Ti has a small, reversible areal CSC of 0.032 ± 0.02 mF/cm^2. The areal CSC of Ti is attributed solely to charge storage in the EDL

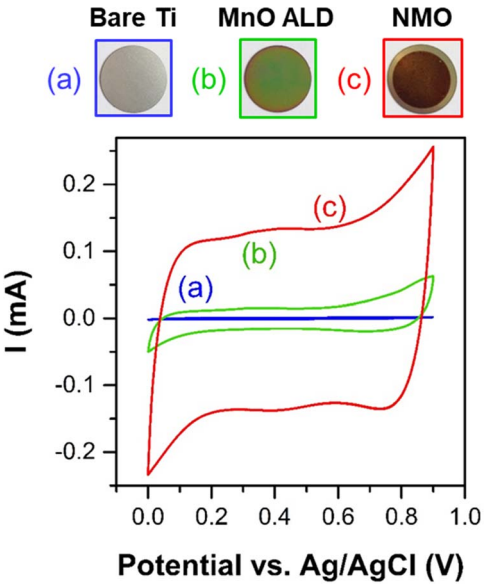

Figure 4. Electrochemical conversion of MnO to NMO. Cyclic voltammetry (CV) and corresponding photographs of substrate, MnO and NMO films. (a) A bare titanium substrate, (b)) a thin film of MnO deposited on titanium via 500 cycles of ALD, and (c) the same thickness of MnO film electrochemically oxidized to NMO in $NaCl_{(aq)}$. CV scans were measured in 0.1 M NaCl at 20 mV/s using a three-electrode setup.

at the surface of the flat substrate. MnO coated Ti samples exhibit a somewhat higher CSC. While MnO is not expected to exhibit electrochemical charge storage, previous studies have shown that ALD MnO films form a thin surface layer of MnO_2.[25] The higher CSC of MnO-coated Ti samples may be attributed to this surface MnO_2. Following electrochemical conversion to NMO, these films have a much higher CSC. Compared to bare Ti, NMO coatings have a thickness-dependent increase in areal capacitance by a factor of up to 170. Given the consistency in behavior between conversion in $Na_2SO_{4(aq)}$ and $NaCl_{(aq)}$, the CSC increase shown in Figure 4 is likely due to Na^+-mediated charge storage in NMO.[12,13]

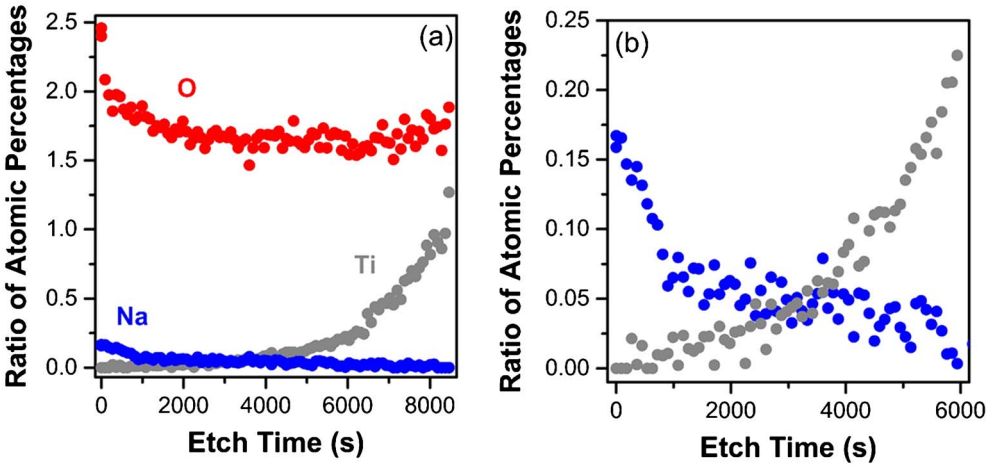

Figure 5. XPS depth profile of NMO. An XPS depth profile using Ar^+ sputtering reveals the composition of a NMO film with an initial MnO ALD thickness of 817 Å. (a) Ratios of atomic percentages are given with respect to Mn. The O:Mn ratio close to 2 throughout the film is consistent with total conversion of the MnO film to a higher oxidation state. (b) A zoomed window of (a) highlighting the bulk Na concentration. A detectable concentration of Na is present throughout the film, with a higher concentration toward the surface.

Verifying Na-mediated charge storage.—XPS depth-profiling was used to confirm the incorporation of Na into NMO formed in $NaCl_{(aq)}$. XPS shows Na incorporation at the surface and in the near-surface bulk of the NMO film, as depicted in Figure 5. Depth profiling reveals an O:Mn ratio > 1.5 through the entire thickness of an 81.7 nm film. The near-surface ∼14 nm of the film has an O:Mn ratio of 2.1, whereas the ∼68 nm bulk of the film has a slightly lower oxygen content ratio of 1.6. Similarly, the surface of the film has a higher Na content than the bulk. Shown in Figure 5b, the bulk of the film has a Na:Mn ratio of 0.06, while the near-surface ∼14 nm has a higher Na content, and a maximum Na:Mn ratio of 0.17. Together, XPS depth-profiling suggests a surface composition of $Na_{0.17}MnO_2$ and a bulk composition of $Na_{0.5}Mn_5O_8$.

Both surface and bulk compositions of our NMO films have a lower concentration of Na than the $Na_{0.44}MnO_2$ particles used in previous HCDI studies.[6,7,18–20] Additionally, O and Na concentrations in these films are lower than those of our previous work where electrochemical conversion was performed in $Na_2SO_{4(aq)}$. Films converted in Na_2SO_4 had a more uniform Na:Mn ratio of 0.25 and an O:Mn ratio of 2.[13] The discrepancy in elemental composition can be attributed to incomplete conversion of the film in the $NaCl_{(aq)}$ electrolyte used here. We suspect that $Cl^-_{(aq)}$ oxidation to $Cl_{2(g)}$ at 0.75 V vs. Ag/AgCl competes with oxidation of MnO to NMO at this pH during NMO formation. As shown in the following sections, incomplete conversion somewhat limits CSC of NMO oxidized in $NaCl_{(aq)}$ as compared to NMO oxidized in $Na_2SO_{4(aq)}$.[13] However, the presence of Na both at the surface and in the bulk of the NMO film support Na incorporation into the film during electrochemical oxidation in $NaCl_{(aq)}$ and suggest that, with some additional refinement, these NMO films could be effective for electrochemical removal of Na^+ in HCDI.

Optimizing NMO film thickness.—To understand the depth to which charge storage occurs in NMO, we vary the thickness of the starting MnO film and evaluate the areal CSC of the resulting NMO films following electrochemical conversion in $NaCl_{(aq)}$, as shown in Figure 6. The ability to tune film thickness and thereby reduce unused bulk material is one advantage of thin films over particulate NMO in these systems. As shown in Figure 6a, the areal CSC increases with the initial MnO film thickness, as more bulk material is available for charge storage. However, the areal CSC reaches an upper limit at an initial MnO thickness of 45 nm, after which thicker films do not provide additional charge storage. This behavior suggests that cation intercalation into the bulk of the film contributes little to the CSC. We observed similar thickness-dependent charging behavior in prior work for NMO converted in $Na_2SO_{4(aq)}$.

The highest specific mass CSCs (F/g) are observed for the thinnest initial MnO ALD films, as shown in Figure 6b. Specific mass CSC values are normalized to a calculated mass of post-processed MnO_2, assuming complete conversion of MnO to MnO_2 and thickness of MnO ALD films as measured by spectroscopic ellipsometry. This is a conservative estimate considering the partial conversion observed by XPS in Figure 5. The highest specific mass CSC calculated was 309 ± 48 F/g at a sweep rate of 20 mV/s for films as thin as 5.4 nm. Specific mass CSC decreases with film thickness, indicating that the majority of charge storage occurs at or near the surface of the NMO film following conversion in $NaCl_{(aq)}$. The confinement of sodium insertion to the surface of these films is likely a product of the limited electrochemical conversion, as described above. More uniform charge storage throughout the thickness of the film may be achieved by converting films in $Na_2SO_{4(aq)}$, as previously described,[13] or by developing techniques for direct growth of NMO.

HCDI using thin-film NMO.—High surface area CNT electrodes were used for desalination testing. These electrodes ensure a large EDL and mimic the standard CDI cell configuration. We compare two configurations – a conventional CDI cell with symmetric CNT electrodes (CNT/CNT), and an HCDI cell with a NMO-coated CNT cathode and Ag-decorated CNT anode (NMO-CNT/Ag-CNT). The HCDI cathode was comprised of CNTs coated with 125 ALD cycles of MnO, electrochemically oxidized to NMO prior to cell assembly. The initial MnO coating was ∼ 26 nm as measured by XRR on a silicon witness wafer. The 26 nm thickness is expected to provide both a large areal and specific CSC based on the results in Figure 6.

To study the effects of adding a high capacity material to the cathode for Na^+ insertion, as we have done here, the HCDI anode must have an equivalent capacity and rate for anion uptake during desalination experiments. A low capacity or kinetically slow anode will limit the cathode performance. To avoid imposing capacity or rate limits on the NMO-coated CNT cathode, an excess of Ag nanopowder was mixed into the CNT anode in the HCDI cell. Ag particles have been employed for Cl^- sorption electrodes in a number of earlier electrochemical studies.[5,6,48–50] Ag reacts with Cl^- ions under applied bias to form insoluble AgCl, according to

$$Ag_{(s)} + Cl^-_{(aq)} \rightarrow AgCl_{(s)} + e^-.$$

We note that Ag is not a cost-effective HCDI anode material for scale-up. Additionally, AgCl formation has limited reversibility due to the increased electrical resistance of AgCl,[6] leading to a poor cycle lifetime. Furthermore, Ag nanoparticles and the Ag^+ ion are toxic, making them undesirable for water purification systems.[51,52] Despite

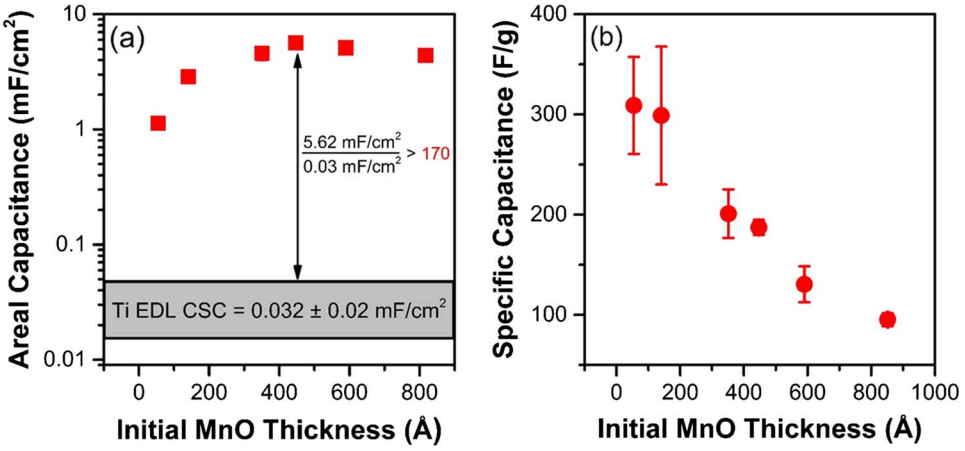

Figure 6. Tuning NMO film thickness for enhanced capacity. Capacitance measurements at a sweep rate of 20 mV/s of post-oxidized NMO films versus the starting film thickness of the pre-oxidized ALD MnO film. (a) Capacitance of NMO films normalized to the area of the film. Areal capacitance increases with film thickness up to 44.8 nm, where thicker films do not contribute additional charge storage. (b) Capacitance normalized to film mass is negatively correlated with film thickness, with the highest specific capacities of ∼300 F/g at 5.4 and 14.0 nm.

its shortcomings, Ag is the most well-studied material for electrochemical anion incorporation in HCDI devices. We used Ag nanoparticles here to study NMO films as HCDI cathodes, and a molar excess was used to ensure that the cathode performance was not artificially limited.

Desalination tests were performed in a constant potential configuration. Potential was step-cycled between 0.0 and 1.0 V across the two-electrode cell. We note that the CDI and HCDI cells are expected to have different desalination profiles. In the CNT/CNT CDI configuration, desalination occurs during the 1.0 V half cycle and electrode regeneration occurs during the 0.0 V half cycle. However, in the NMO-CNT/Ag-CNT HCDI configuration, electrode regeneration occurs during the 1.0 V half cycle and desalination occurs during the 0.0 V half cycle, as depicted in Figure 1. During the 1.0 V half cycle, the nominal half reactions in the HCDI cell are

$$NaMn_4O_8 \rightarrow Na^+_{(aq)} + e^- + Mn_4O_8$$

and

$$AgCl + e^- \rightarrow Ag + Cl^-_{(aq)},$$

to yield the overall regeneration reaction

$$NaMn_4O_8 + AgCl \rightarrow Mn_4O_8 + Ag + NaCl_{(aq)}.$$

During the 0.0 V half cycle, the nominal half reactions reverse to yield the overall desalination reaction

$$Mn_4O_8 + Ag + NaCl_{(aq)} \rightarrow NaMn_4O_8 + AgCl.$$

For both cells, one cycle consisted of 1.0 V held for 15 minutes and 0.0 V held for 15 minutes for a total of 30 minutes per cycle. We note that cycle times were set to ensure sufficient time for complete desalination and regeneration for characterization purposes. Cycle times could be shortened in future operation to obtain precise rates of desalination. We report CSC and SSC values after eight charge-discharge conditioning cycles. At this point, salt sorption and desorption are within 4% variation, and are averaged over five cycles of desalination/regeneration. See SI Section K for salt sorption and charge transfer values for all five cycles. Electrode stability over hundreds of cycles is necessary for commercial desalination devices and is currently not achievable with the materials studied here under electrolyte flow, but is the subject of ongoing effort.

Consistent with results observed on flat electrodes, charge storage behavior is starkly different between the HCDI and CDI cells, as shown in Figure 7. During the 1.0 V half cycle, the CDI carbon electrode cell had an average capacity of 58.4 ± 0.9 mC. In contrast, the HCDI cell had an average capacity of 1.3380 ± 0.0200 C, a factor of ∼23 increase in charge storage-capacity over the CDI cell. During

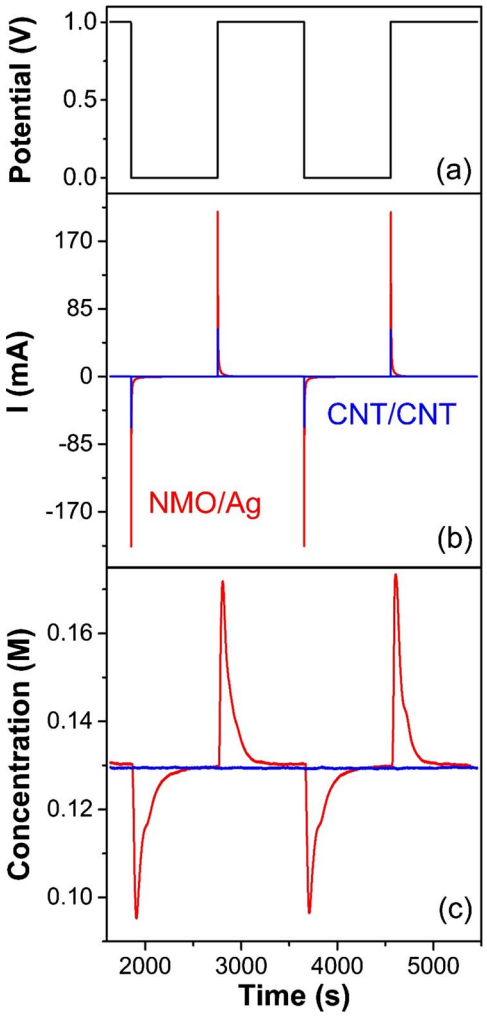

Figure 7. Desalination performance of CNT electrodes. Plot of (a) potential, (b) current, and (c) effluent salt concentration versus time during electrochemical desalination for HCDI (NMO-CNT/Ag-CNT) and CDI (CNT/CNT) configurations. Desalination performance of the HCDI cell shows a > 20-fold enhancement in charge storage over the CDI configuration during desalination and regeneration, and produces a charging efficiency > 100%.

the 0.0 V half-cycle, an even larger increase in charge storage over the CDI cell is observed. The CDI cell averages -21.3 ± 0.1 mC, while the HCDI cell averages -1.2459 ± 0.0123 C. The increase in charge storage during the 0.0 V half-cycle is 58 times greater in the HCDI cell than in the CDI cell. The advantage of the HCDI cell is also reflected in the coulombic efficiency of 93% for the HCDI cell versus 37% for the CDI cell over these five desalination cycles. The high coulombic efficiency of the HCDI cell suggests a reversible process with a low net energy consumption.

The stark increase in CSC in the HCDI cell is reflected by an increase in SSC, as seen in the concentration profile of the effluent solution during cycling in Figure 7. For the HCDI cell, we observe dramatic changes in the effluent salt concentration with transient decreases in salt concentration of > 0.03 M below the inlet salt concentration. In contrast, differences in salt concentration are below the detection limit of the conductivity meter for the CDI cell. In the HCDI cell, 0.93 ± 0.03 mg of salt was removed per cycle during the 0 V step.

We expect the CSC of the cathode to be ~250 F/g, based on the 26 nm thickness of the MnO coating on a silicon witness wafer and the specific capacity results in Figure 6b. For a 1V charging potential, this is equal to 69.4 mAh/g. Based on this CSC, the theoretical SSC of the NMO is 151 mg_{NaCl} $(g_{NMO})^{-1}$. With an anode of equivalent CSC to our NMO-based cathode, the normalized SSC would be ~ 75 mg g^{-1}, a value well above the highest reported HCDI SSC.[7] Assuming a conformal MnO film on the CNT-OH powder with 200 m^2/g surface area and 100% conversion to NMO, the mass of NMO in the HCDI cathode is estimated to be 87 mg. We expect the actual mass loading to be lower than this due to diffusion limitations of the gas phase precursors into the CDI electrodes, and mass loss during the electrochemical conversion to NMO. The average measured amount of salt removed in the HCDI cell was 0.93 ± 0.03 mg per cycle. Assuming an NMO mass of 87 mg yields an experimental SSC of 11 ± 0.3 mg_{NaCl} $(g_{NMO})^{-1}$. Normalizing experimental salt removal to the mass of both electrodes (a CDI convention) yields a SSC of 5.6 ± 0.2 mg_{NaCl} $(g_{total\ electrode})^{-1}$ for the HCDI cell, a value lower than the highest reported values for an HCDI system (31.2 mg_{NaCl} $(g_{electrode})^{-1}$) and for a conventional CDI system (14.9 mg_{NaCl} $(g_{electrode})^{-1}$).[7,53] These relatively low values might be due to (1) incomplete coating of the CNT-OHs, (2) incomplete conversion to NMO, and (3) the large overpotential to regenerate Ag from AgCl. A higher SSC may be achieved with further optimization of the deposition and conversion processes, as well as the use of an easily regenerated high capacity anode.

Despite these low SSC values, our HCDI cell shows high charging efficiency ($\wedge$) values. $\wedge$ (mol NaCl/mol e^-) values are conventionally below 100% in CDI literature. In our HCDI cell, we measure surprisingly high $\wedge$ values of 123 ± 5% for the 0 V half-cycle (desalination), and 115 ± 6% for the 1.0 V half-cycle (regeneration) over five cycles of charge/discharge. For comparison, the highest reported $\wedge$ value for a HCDI system using NMO is 82%, and for a CDI system is close to unity.[19,54] These anomalously high $\wedge$ values are reversible on both charge and discharge steps over multiple cycles.

We examined a range of common experimental artifacts and known physical phenomena which could potentially contribute to these high charging efficiencies, but these factors did not account for the charging behavior we observed. We considered, for instance, (1) reduced co-ion expulsion arising from high ion-selectivity of the electrode materials, (2) progressive wetting, (3) static charge build up in the electrodes before operation, (4) side reactions, for example to form Cl_2, (5) decomposition of manganese oxide during cycling leading to flocculation and removal of ions, and (6) pH changes arising from generation of H^+ or OH^- during operation.[3,55–58] However, none of these alternative effects or combinations thereof satisfactorily explain the behavior we observe.

Reduced co-ion expulsion could explain $\wedge$ approaching 100%,[3,4,59] but does not account for $\wedge > 100$%. Static charge buildup and progressive wetting are expected to dissipate during the pretreatment procedures we describe above (overnight soaking in electrolyte and seven forming cycles) and are not expected to remain during cycles 8–13 as we observe. Furthermore, irreversible processes like progressive wetting, static charge buildup, Cl_2 formation, flocculant formation, or conductivity increases arising from H^+ or OH^- generation would be expected to result in $\wedge > 100$% for only one half cycle (either charge or discharge) yielding low coulombic efficiencies, whereas we observe $\wedge > 100$% for both charge and discharge cycles over five cycles with coulombic efficiencies of 93%. We also note that if H^+ or OH^- were catalytically or electrochemically generated on the electrode surface, the conductivity of the effluent solution would be expected to plateau to a constant value arising from a constant rate of production of H^+ or OH^-. Instead, we observe spikes with an exponential decrease for both charge and discharge steps in Figure 7c, consistent with desalination and regeneration. In an effort to understand this high efficiency, we employed EQCM and ab initio modeling as discussed in the following text, which provide mechanistic support for the high charging efficiency we observed in HCDI cell tests.

The relationship between charge storage and ion removal in NMO.—EQCM was used to probe the contribution of reversible Na^+ sorption to the CSC of NMO. In EQCM, a quartz crystal serves as both mass sensor and working electrode. EQCM results for a ~ 40 nm thick NMO film in 0.10 M $NaCl_{(aq)}$ electrolyte are shown in Figure 8 during CV operation. These results reveal a mass loss associated with an anodic current, as potential is swept from 0 to 0.9 V vs Ag/AgCl, and a mass gain associated with a cathodic current, as potential is reversed and swept from 0.9 to 0 V vs Ag/AgCl. This behavior is qualitatively consistent with cation insertion into the NMO film as identified above with XPS and HCDI testing, and is also consistent with previous work from our group on electrochemical Na^+ insertion in NMO.[13] We note that the only ions in solution are Na^+ and Cl^- and the experiments were carried out at a circumneutral pH. Therefore we expect that the cation mediated charge storage we observe arises from Na^+.

We further evaluated our EQCM data to quantitatively compare the changes in mass and charge during CV measurements. Mass changes were calculated from shifts in the EQCM resonance frequency. Charge was calculated from the integral under the CV curve. The total charge transferred, Q, while sweeping over a potential range, ΔV, is calculated as $Q = CSC \times \Delta V$, where $\Delta V = 0.9$ V. A mass-to-charge ratio is calculated by taking the mass change on the oxidizing sweep from Figure 8b divided by the charge transferred during the oxidizing sweep in Figure 8a. For stoichiometric incorporation of Na^+, with one electron transferred per ion sorbed, the normalized mass-to-charge ratio measured by EQCM is expected to correspond to the molar mass of Na^+ (23 g/(mol e^-)). However, we measure larger mass-to-charge ratios. Over the entire 0.9 V cycling window we measure an average mass-to-charge ratio of 49 g $(mol\ e^-)^{-1}$.

In Figure 8a we observe a relatively constant current of ~ 0.08 mA over the full potential range from 0–0.9 V vs. Ag/AgCl. However, we observe two distinct regions in the EQCM plot in Figure 8b. From 0.0–0.4 V vs Ag/AgCl, we observe a slope of 3.0 μg/V in Figure 8b, corresponding to a mass-to-charge ratio of 68 g $(mol\ e^-)^{-1}$. In contrast, from 0.5–0.9 V vs Ag/AgCl, we observe a slope of 0.8 μg/V in Figure 8b, corresponding to a lower mass-to-charge ratio of 17 g $(mol\ e^-)^{-1}$. These trends in mass change are consistent with those observed for NMO formed in $Na_2SO_{4(aq)}$.[13]

In our prior work, we attributed measured EQCM mass-to-charge ratios exceeding 23 g/(mol e^-) in NMO to non-ideal Sauerbrey behavior arising from viscoelastic dissipation in the NMO films.[13] However, the anomalously high desalination charging efficiency measured for these NMO electrodes during HCDI testing caused us to reevaluate this assumption and identify an alternative explanation — namely a decoupling of electron and ion transfer in NMO. To help understand what gives rise to the two distinct regions of the slope measured by EQCM in Figure 8b we used ab initio modeling, as described below and in the SI.

Using the UEB construct as discussed in the methods section, we are able to separately predict the thermodynamic favorability of electron transfer and ion transfer. Previous work from our group used

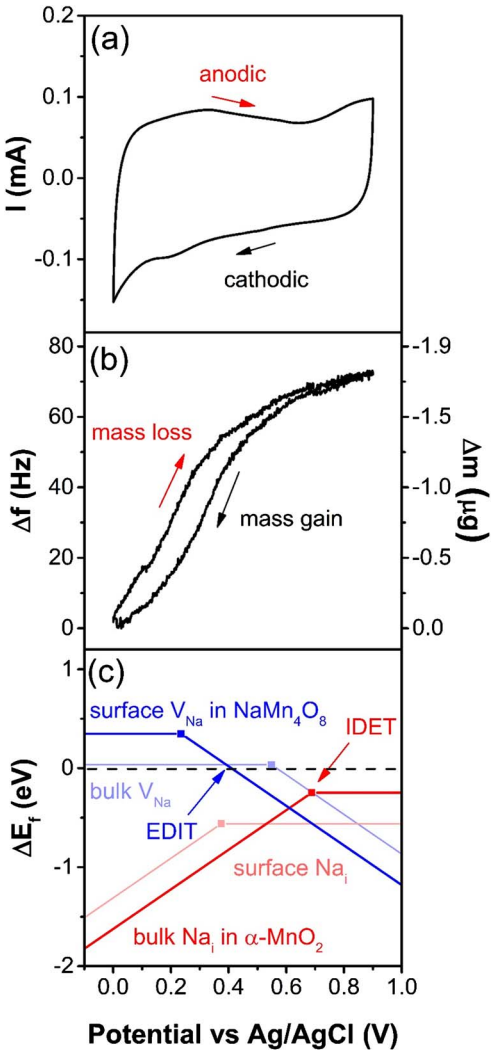

Figure 8. Decoupled ion and electron transfer in NMO films. (a) CV measured during EQCM of 400 ALD cycles of MnO oxidized to NMO, performed at 20 mV/s in 0.1 M NaCl, (b) EQCM frequency shifts indicate a reversible mass gain as the potential sweeps negatively and a mass loss as the potential sweeps back positively. (c) Ab initio modeling describing the bounding limits of behavior possible in NMO: V_{Na} in $NaMn_4O_8$ and Na_i in α-MnO_2 at surface and bulk conditions. EQCM and modeling results are consistent with surface EDIT in NMO at potentials < 0.4 V vs. Ag/AgCl.

this construct to explore decoupled ion and electron transfer leading to high rate electronic charge storage.[12,13,28] Here, ab initio modeling suggests a previously undescribed mechanism of electron decoupled ion transfer (EDIT) at the surface of NMO. Presented in Figure 8c are surface and bulk descriptions of defect formation energy versus potential for a sodium interstitial (Na_i) in α-MnO_2 and a sodium vacancy (V_{Na}) in $NaMn_4O_8$ calculated using ab initio modeling. These phases were chosen as reference boundaries of the range of possible thermodynamic behavior expected for NMO in this work. However, we note that the NMO films described experimentally are not crystalline and therefore may exhibit some variation in electrochemical behavior. In Figure 8c ion transfer is predicted to occur when the potential is swept over a region where the defect formation energy transitions between favorable ($\Delta E_f < 0$) and unfavorable ($\Delta E_f > 0$), and electron transfer is predicted when the potential is swept over a region where the defect is predicted to change charge state (indicated by a kink in each trace of ΔE_f vs. potential, marked with a symbol). For further explanation of these methods see the SI section L and Ref. 13.

The model predictions for the surface description of $NaMn_4O_8$ in Figure 8c are the most illuminating for understanding our experimental observations of mass-to-charge ratios exceeding 23 g/(mol e^-) in NMO. Considering the near-surface Na:Mn ratios of up to 0.17 in these films as measured by XPS in Figure 4, the surface description of a sodium vacancy (V_{Na}) in sodium-rich $NaMn_4O_8$ (i.e. conversion of $Na_{0.25}MnO_2$ to form $Na_{0.19}MnO_2$) is expected to be more relevant to the experimental measurements. This surface trace for V_{Na} in $NaMn_4O_8$ in Figure 8c suggests the possibility of a previously undescribed phenomenon.

As the potential is swept < 0.4 V vs. Ag/AgCl in Figure 8c, Na^+ is predicted to transfer into Na-deficient $Na_{1-x}Mn_4O_8$, but the corresponding electron transfer is not predicted to occur until a potential < 0.2 V vs. Ag/AgCl. If the potential sweep is reversed toward positive potentials without applying a potential < 0.2 V, Na^+ is predicted to transfer back out of $NaMn_4O_8$ without an electron transfer having occurred. In other words, some fraction of Na^+ may undergo potential-dependent sorption into $Na_{1-x}Mn_4O_8$ over the potential range of 0.2–0.4 V vs. Ag/AgCl without a corresponding electron transfer. Here we refer to this phenomenon of ion transfer without stoichiometric electron transfer as "electron-decoupled ion transfer," or "EDIT."

When coupled with these ab initio predictions, the EQCM results in Figure 8 suggest that the EDIT mechanism may be occurring in NMO. In Figure 8, we cycle the potential from 0–0.9 V vs. Ag/AgCl and measure an average mass-to-charge ratio of 49 g (mol e^-)$^{-1}$ by EQCM, corresponding to 2.1 Na^+/e^-. Over a narrower potential window of 0–0.4 V vs. Ag/AgCl this mass-to-charge ratio is even higher, corresponding to 3.0 Na^+/e^-. In comparison, an uncoated EQCM electrode exhibits sub-stoichiometric sorption of 0.5 Na^+/e^- (Figure S3), which we attribute to the formation of the EDL.

For the NMO electrode, over this potential range we expect to observe the superposition of (1) the formation of the EDL at the surface of the NMO and CNTs, (2) conventional faradaic intercalation of Na^+ into bulk NMO, (3) the EDIT mechanism in near-surface NMO. For conventional faradaic intercalation, a mass-to-charge ratio of 23 g (mol e^-)$^{-1}$, or 1 Na^+/e^- is expected. The value of 2.1 Na^+/e^- we measure by EQCM suggests that EDIT may contribute in the potential range of 0 – 0.9 V vs. Ag/AgCl in our system. In the potential range where EDIT is predicted to dominate (0.2–0.4 V vs. Ag/AgCl), we observe the largest mass-to-charge ratio, corresponding to 3.0 Na^+/e^-. This ab initio description of EDIT provides an explanation for the EQCM results and the high HCDI efficiency we observe.

The EDIT mechanism, and corresponding values of $\wedge > 100\%$ that we observe are surprising. In CDI literature, $\wedge$ is assumed to have a theoretical maximum of 100%, and co-ion desorption is assumed to give rise to values consistently < 100%.[59–61] However, by our understanding, the limit of $\wedge \leq 100\%$ is not rooted in a thermodynamic barrier, but in an assumption of charge balance.

We note that the EDIT mechanism we propose is predicted to be restricted to the surface of NMO and is expected to have a limited contribution in bulk NMO. Because our work uses thin films of NMO, there is an increased contribution from EDIT over other experimental studies using larger-size NMO particles. EDIT may also help explain larger-than-stoichiometric mass-to-charge ratios which have been noted in other nanoscale materials during electrochemical operation, including thin-film MnO_2 [13] and nanoporous carbon.[62,63] In these prior studies, charge balance was assumed apriori, and anomalous mass-to-charge ratios were attributed to solvent or dissipation effects. Here, we were able to more directly probe the origin of these effects with simultaneous electrochemical measurements and effluent salt concentration measurements. This measurement capability allowed us to identify behavior consistent with EDIT.

The EDIT behavior our data supports may bring into question the apriori assumption of local charge balance for cation insertion electrochemistry in a larger sense. Charge self-regulation in transition metal semiconductors[64–67] is expected to be able to stabilize electronic and/or ionic charge in host structures, giving rise to EDIT behavior. Ultimately, our work suggests that the ion and electron transfer should

be examined independently in transition-metal semiconductors. Our work also calls for further study of transition metal semiconductor electrochemistry in a range of electrochemical applications to evaluate the possibility of decoupled electron and ion transfer.

In the current work, we demonstrate a valuable set of experimental tools for understanding these effects. However, further experimental tools should be developed to independently probe mass and charge changes in electrode materials and electrolytes during electrochemical cycling. By harnessing and enhancing the EDIT effect with improved cycling stability, we expect to achieve new levels of efficiency and rate in electrochemical desalination.

Conclusions

In this work we demonstrate the successful conversion of thin-film MnO to electrochemically active NMO in $NaCl_{(aq)}$. XPS results indicate that conversion to NMO in $NaCl_{(aq)}$ is limited to the near-surface. Despite this, NMO films formed in $NaCl_{(aq)}$ exhibit charge storage capacities up to 170 times higher than uncoated electrodes. We observe the highest specific mass capacitances for the thinnest films, with values of ∼300 F/g measured for 5.4 and 14.0 nm films. The highest areal capacitance of 5.62 mF/cm^2 was measured for a 44.8 nm film thickness. These results suggest that, with further optimization, HCDI devices could be deployed with electrodes coated with 5–50 nm MnO films, which can be converted in operando in water containing NaCl to form NMO for enhanced desalination performance.

We also report on an initial study of the desalination performance of thin film NMO. We study early cycling data of an HCDI cell comprised of a NMO-coated CNT cathode and an Ag nanoparticle-decorated CNT anode. We compare this HCDI cell to a CDI cell comprised of symmetric CNT electrodes that model conventional CDI operation. The HCDI configuration exhibits a >20-fold increase in charge storage and dramatically improves desalination performance compared to the symmetric CDI configuration. We also observe an anomalously high charging efficiency (mol NaCl (mol e-)$^{-1}$) of up to 123 ± 5%, which cannot be explained by experimental artifacts or known physical phenomena. This charging efficiency of $\wedge > 100\%$ is unprecedented, and if validated, harnessed and refined for use in full-scale HCDI devices, promises to enable new levels of energy efficient desalination.

Additionally, EQCM and ab initio modeling results support the high charging efficiency we measure in desalination tests. Over the potential range of 0 – 0.9 V vs. Ag/AgCl, EQCM data suggests the removal of 2.1 Na^+/e^-, with as many as 3.0 Na^+/e^- removed over the range of 0 – 0.4 V vs. Ag/AgCl. This behavior is corroborated by ab initio computational results using the UEB framework, capturing a phenomenon we term electron-decoupled ion transfer, or "EDIT." EDIT is predicted to occur at the surface of NMO, and is enhanced in the thin-film NMO coatings used in this work. The EDIT mechanism challenges the common assumption of local charge balance in HCDI electrodes. If the EDIT mechanism proves correct, then this mechanism could enable unforeseen levels of energy efficiency in HCDI. We suggest that this mechanism may also be at play in other ion-insertion electrode materials, and that new materials could be designed to enhance this effect for improved HCDI efficiency.

Acknowledgments

This research was funded by the DOE SBIR grant titled "Enhanced Capacitive Deionization Using Carbon Electrodes Conformally Coated with Metal Oxide by Atomic Layer Deposition" through a subcontract from ALD NanoSolutions, Inc. M.J.Y. acknowledges the National Research Council for a Research Associateship award at the National Institute of Standards and Technology, and partial support as part of the Joint Center for Energy Storage Research (JCESR), an Energy Innovation Hub funded by the U.S. Department of Energy (DOE), Office of Science, Basic Energy Sciences (BES). We thank Edwin Heilweil and the Raritan Cluster Steering Group at the National Institute of Standards and Technology for assistance with ab initio computational modeling. We also acknowledge Integrated Instrument Development Facility at the University of Colorado Boulder for assistance in electrochemical cell design and fabrication.

ORCID

Jasmine M. Wallas https://orcid.org/0000-0001-6794-1671
Matthias J. Young https://orcid.org/0000-0001-7384-4333
Huaxing Sun https://orcid.org/0000-0002-8638-4492
Steven M. George https://orcid.org/0000-0003-0253-9184

References

1. W. A. Jury and H. Vaux, *Proc. Natl. Acad. Sci. U. S. A.*, **102**(44), 15715 (2005).
2. LIGTT. *50 Breakthroughs: Critical scientific and technological advances needed for sustainable global development*, LBNL Institute for Globally Transformative Technologies: Berkeley, CA, 2014.
3. S. Porada, R. Zhao, A. van der Wal, V. Presser, and P. M. Biesheuvel, *Prog. Mater. Sci.*, **58**(8), 1388 (2013).
4. M. E. Suss, S. Porada, X. Sun, P. M. Biesheuvel, J. Yoon, V. Presser, M. Biesheuvel, J. Yoon, and V. Presser, *Energy Environ. Sci.*, **8**(8), 2296 (2015).
5. F. La Mantia, M. Pasta, H. Deshazer D., B. E. Logan, and Y. Cui, *Nano Lett.*, **11**(4), 1810 (2011).
6. M. Pasta, C. D. Wessells, Y. Cui, and F. La Mantia, *Nano Lett.*, **12**(2), 839 (2012).
7. J. Lee, S. Kim, C. Kim, and J. Yoon, *Energy Environ. Sci.*, **7**(11), 3683 (2014).
8. B. E. Conway, *J. Electrochem. Soc.*, **138**(6), 1539 (1991).
9. Y. Cao, L. Xiao, W. Wang, D. Choi, Z. Nie, J. Yu, L. V. Saraf, Z. Yang, and J. Liu, *Adv. Mater.*, **23**(28), 3155 (2011).
10. N. Van Nghia, P.-W. Ou, and I.-M. Hung, *Electrochim. Acta*, **161**, 63 (2015).
11. S. Guo, H. Yu, Z. Jian, P. Liu, Y. Zhu, X. Guo, M. Chen, M. Ishida, and H. Zhou, *ChemSusChem*, **7**(8), 2115 (2014).
12. M. J. Young, A. M. Holder, S. M. George, and C. B. Musgrave, *Chem. Mater.*, **27**(4), 1172 (2015).
13. M. J. Young, M. Neuber, A. C. Cavanagh, H. Sun, C. B. Musgrave, and S. M. George, *J. Electrochem. Soc.*, **162**(14), A2753 (2015).
14. L. Mai, H. Li, Y. Zhao, L. Xu, X. Xu, Y. Luo, Z. Zhang, W. Ke, C. Niu, and Q. Zhang, *Sci. Rep.*, **3**, 1718 (2013).
15. P. Simon and Y. Gogotsi, *Nat. Mater.*, **7**(11), 845 (2008).
16. Y. Yuan, C. Zhan, K. He, H. Chen, W. Yao, S. Sharifi-Asl, B. Song, Z. Yang, A. Nie, X. Luo, H. Wang, S. M. Wood, K. Amine, M. S. Islam, J. Lu, and R. Shahbazian-Yassar, *Nat. Commun.*, **7**, 13374 (2016).
17. D. Chen, D. Ding, X. Li, G. H. Waller, X. Xiong, M. A. El-Sayed, and M. Liu, *Chem. Mater.*, **27**(19), 6608 (2015).
18. K. C. Smith and R. Dmello, *J. Electrochem. Soc.*, **163**(3), A530 (2016).
19. J. Yang, L. Zou, H. Song, and Z. Hao, *Desalination*, **276**(1–3), 199 (2011).
20. J. Yang, L. Zou, and H. Song, *Desalination*, **286**, 108 (2012).
21. M. Toupin, T. Brousse, and D. Bélanger, *Chem. Mater.*, **16**(16), 3184 (2004).
22. W. Yan, J. Y. Kim, W. Xing, K. C. Donavan, T. Ayvazian, and R. M. Penner, *Chem. Mater.*, **24**(12), 2382 (2012).
23. Y. S. Jung, A. S. Cavanagh, L. A. Riley, S.-H. Kang, A. C. Dillon, M. D. Groner, S. M. George, and S.-H. Lee, *Adv. Mater.*, **22**(19), 2172 (2010).
24. *Seawater Corrosion Handbook*, M. Schumacher, Ed.; Noyes Data Corporation: Park Ridge, New Jersey, 1979.
25. B. B. Burton, F. H. Fabreguette, and S. M. George, *Thin Solid Films*, **517**(19), 5658 (2009).
26. S. J. Martin, V. E. Granstaff, and G. C. Frye, *Anal. Chem.*, **63**(20), 2272 (1991).
27. S. J. Martin, J. J. Spates, K. O. Wessendorf, T. W. Schneider, and R. J. Huber, *Anal. Chem.*, **69**(11), 2050 (1997).
28. M. J. Young, H.-D. Schnabel, A. M. Holder, S. M. George, and C. B. Musgrave, *Adv. Funct. Mater.*, **26**(43), 7895 (2016).
29. P. E. Blöchl, *Phys. Rev. B*, **50**(24), 17953 (1994).
30. G. Kresse and J. Furthmüller, *Phys. Rev. B*, **54**(16), 11169 (1996).
31. G. Kresse and D. Joubert, *Phys. Rev. B*, **59**(3), 1758 (1999).
32. J. Perdew, K. Burke, and M. Ernzerhof, *Phys. Rev. Lett.*, **77**(18), 3865 (1996).
33. A. Alkauskas and A. Pasquarello, *Phys. Rev. B*, **84**(12), 125206 (2011).
34. G. Pacchioni, *J. Chem. Phys.*, **128**(18), 182505 (2008).
35. L. Schimka, J. Harl, and G. Kresse, *J. Chem. Phys.*, **134**, 24116 (2011).
36. D. M. Sherman, *Geochim. Cosmochim. Acta*, **69**(13), 3249 (2005).
37. W. Tan, S. Lu, F. Liu, X. Feng, J. He, and L. K. Koopal, *Soil Sci.*, **173**(4), 277 (2008).
38. C. J. Fall, N. Binggeli, and A. Baldereschi, *J. Phys. Condens. Matter*, **11**(13), 2689 (1999).
39. J. P. Perdew, A. Ruzsinszky, G. I. Csonka, O. A. Vydrov, G. E. Scuseria, L. A. Constantin, X. Zhou, and K. Burke, *Phys. Rev. Lett.*, **100**(13), 136406 (2008).
40. V. Stevanović, S. Lany, D. S. Ginley, W. Tumas, and A. Zunger, *Phys. Chem. Chem. Phys.*, **16**(8), 3706 (2014).
41. S. Porada, M. Bryjak, A. van der Wal, and P. M. Biesheuvel, *Electrochim. Acta*, **75**, 148 (2012).
42. S. Porada, L. Borchardt, M. Oschatz, M. Bryjak, J. S. Atchison, K. J. Keesman, S. Kaskel, P. M. Biesheuvel, and V. Presser, *Energy Environ. Sci.*, **6**(12), 3700 (2013).
43. S. Yang, S. Jeon, H. Kim, J. Choi, J. Yeo, H. Park, and D. K. Kim, *ACS Sustain. Chem. Eng.*, **4**(8), 4174 (2016).

44. A. S. Cavanagh, C. A. Wilson, A. W. Weimer, and S. M. George, *Nanotechnology*, **20**(25), 255602 (2009).
45. J. Ferguson, A. Weimer, and S. George, *Thin Solid Films*, **371**(1), 95 (2000).
46. J. A. McCormick, B. L. Cloutier, A. W. Weimer, and S. M. George, *J. Vac. Sci. Technol. A Vacuum, Surfaces, Film.*, **25**(1), 67 (2007).
47. A. Zydor and S. D. Elliott, *J. Phys. Chem. A*, **114**(4), 1879 (2010).
48. M. Pasta, A. Battistel, and F. La Mantia, *Energy Environ. Sci.*, **5**(11), 9487 (2012).
49. J. Lee, S.-H. Yu, C. Kim, Y.-E. Sung, and J. Yoon, *Phys. Chem. Chem. Phys.*, **15**(20), 7690 (2013).
50. S. Kim, J. Lee, C. Kim, and J. Yoon, *Electrochim. Acta*, **203**, 265 (2016).
51. M. Metian and M. Warnau, *Bull. Environ. Contam. Toxicol.*, **81**(5), 455 (2008).
52. J. Fabrega, S. N. Luoma, C. R. Tyler, T. S. Galloway, and J. R. Lead, *Environ. Int.*, **37**(2), 517 (2011).
53. S. Porada, L. Weinstein, R. Dash, A. van der Wal, M. Bryjak, Y. Gogotsi, and P. M. Biesheuvel, *ACS Appl. Mater. Interfaces*, **4**(3), 1194 (2012).
54. T. Kim, J. E. Dykstra, S. Porada, A. van der Wal, J. Yoon, and P. M. Biesheuvel, *J. Colloid Interface Sci.*, **446**, 317 (2015).
55. R. A. Rica, R. Ziano, D. Salerno, F. Mantegazza, and D. Brogioli, *Phys. Rev. Lett.*, **109**(15), 156103 (2012).
56. D. R. Franceschetti and J. R. Macdonald, *J. Appl. Phys.*, **50**(1), 291 (1979).
57. J. W. Murray, *J. Colloid Interface Sci.*, **46**(3), 357 (1974).
58. L. S. Balistrieri and J. W. Murray, *Geochim. Cosmochim. Acta*, **46**(6), 1041 (1982).
59. E. Avraham, Y. Bouhadana, A. Soffer, and D. Aurbach, *J. Electrochem. Soc.*, **156**(6), 95 (2009).
60. P. M. Biesheuvel, *J. Colloid Interface Sci.*, **332**(1), 258 (2009).
61. R. Zhao, P. M. Biesheuvel, H. Miedema, H. Bruning, and A. van der Wal, *J. Phys. Chem. Lett.*, **1**(1), 205 (2010).
62. W.-Y. Tsai, P.-L. Taberna, and P. Simon, *J. Am. Chem. Soc.*, **136**(24), 8722 (2014).
63. M. D. Levi, N. Levy, S. Sigalov, G. Salitra, D. Aurbach, and J. Maier, *J. Am. Chem. Soc.*, **132**(38), 13220 (2010).
64. F. D. M. Haldane and P. W. Anderson, *Phys. Rev. B*, **13**(6), 2553 (1976).
65. C. Wolverton and A. Zunger, *Phys. Rev. Lett.*, **81**(3), 606 (1998).
66. H. Raebiger, S. Lany, and A. Zunger, *Nature*, **453**(7196), 763 (2008).
67. A. C. M. M. Padilha, H. Raebiger, A. R. Rocha, and G. M. Dalpian, *Sci. Rep.*, **6**, 28871 (2016).